High Loading of Transition Metal Single Atoms on Chalcogenide Catalysts

Jianwei Zheng,[1] Konstantin Lebedev,[1] Simson Wu,[1] Chen Huang,[2] Tuğçe Ayvalı,[1] Tai-Sing Wu,[3] Yiyang Li,[1] Ping-Luen Ho,[1] Yun-Liang Soo,[3] Angus Kirkland,[2] and Shik Chi Edman Tsang[1]*

[1]Wolfson Catalysis Centre, Department of Chemistry, University of Oxford, Oxford, OX1 3QR, UK.
[2]Department of Materials, University of Oxford, Oxford, OX1 PH, UK
[3]Department of Physics, National Tsing Hua University, Hsinchu, Taiwan.
Correspondence and requests for materials should be addressed to S.C.E.T. (email: edman.tsang@chem.ox.ac.uk).

KEYWORDS : single atom, high loading, chalcogenide, reverse water gas shift, carbon dioxide hydrogenation

ABSTRACT: Transition metal doped chalcogenides are one of the most important class of catalysts which have been attracting increasing attention for petrochemical and energy related chemical transformations due to their unique physiochemical properties. For practical applications, achieving maximum atom utilization by homogeneous dispersion of metals on the surface of chalcogenides is essential. Herein, we report a detailed study of a deposition method using thiourea coordinated transition metal complexes. This method allows the preparation of a library of a wide range of single atoms including both noble and non-noble transition metals (Fe, Co, Ni, Cu, Pt, Pd, Ru) with a metal loading as high as 10 wt% on various ultrathin 2D chalcogenides (MoS_2, $MoSe_2$, WS_2 and WSe_2). As demonstrated by the state-of-the-art characterization, the doped single transition metal atoms interact strongly with surface anions and anion vacancies in the exfoliated 2D materials, leading to high metal dispersion in the absence of agglomeration. Taking Fe on MoS_2 as a benchmark, it has been found that Fe is atomically dispersed until 10 wt% and beyond this loading, formation of coplanar Fe clusters is evident. Atomic Fe, with a high electron density at its conduction band, exhibits a superior intrinsic activity and stability in CO_2 hydrogenation to CO per Fe compared to corresponding surface Fe clusters and other Fe catalysts reported for reverse water-gas-shift reactions.

INTRODUCTION

Heterogeneous catalysts with highly dispersed transition metal (TM) sites on solid supports are critical for efficient catalysis. Selecting high intrinsic activity on a particular support and increasing active site density are the two main areas available for optimizing catalytic performance.[1] Therefore, creating heterogeneous catalysts with optimum usage of TMs and well-defined catalytic sites is essential for developing cost-effective and green chemical processes. Notably, local coordination environment can significantly affect the physicochemical properties of a single atom (SA).[2,3] In addition, idealised catalysts with uniform SA sites with a specific coordination structure aids our understanding heterogeneous catalysis at the atomic level.

During recent years, the potential advantages of single atom catalysis have been proposed and experimentally explored. Numerous studies have also been exemplified using a variety of synthesis methods for preparing single atom catalysts (SACs).[4-6] The strategies to prepare SACs include reducing the loading amount of TM on supports and using voids to confine the SAs.[7-9] In most cases, the mass loading of TM is usually kept low (below 1.5 wt%) in order to avoid agglomeration and maintain monodisperse isolated TM atoms on the supports, which leads to relatively inferior catalytic performance measured on a gram basis.[10] Moreover, in general, the TM and supports are deliberately chosen to construct a specific coordination environment and lack a reliable and versatile strategy to synthesize SACs using practical processes. Currently, there are several methods to prepare SACs developed from bottom up or top-down strategies both of which have advantages and disadvantages.[11,12]

The developed protocols to synthesize SACs can be classified as either physical or chemical methods. Atomic layer deposition (ALD) technique is a typical physical method to synthesize uniform SAs onto a substrate with high precision. However, ALD generally uses specific gaseous TM atoms and requires a high-quality substrate support i.e. single crystal surface.[13] Other physical methods such as mass-selected soft landing[14], and high temperature shockwave[15] also require specialised instruments with finely controlled atom beams. Moreover, using these methods the SA loading cannot be increased due to severe aggregation problems. In comparison, chemical methods from a bottom up approach are less expensive in their preparation cost and less cumbersome in control. However, limited knowledge of the surface chemistry, anchoring and poor understanding of the metal-support interactions can make these syntheses rather empirical.[16] In addition, the materials produced often contain supported TM species with different sizes ranging from SA to nanoparticles due to weak support interactions, allowing surface Oswald ripening of SAs. Reducing the loading of SA on support is beneficial to preventing this so the commonly reported metal loadings achieved by wet chemical anchoring methods are extremely low. For example, the loading of reported

Pt_1/FeO_x, by wet impregnation was only 0.17 wt%.[17] A photochemical route has been developed to prepare Pd_1/TiO_2 with a claimed high loading of SAs, but the actual loading rarely exceeds 1.5 wt%.[6] Another popular chemical strategy involves the carbonization of metal organic frameworks (MOFs) with dopant metal atoms pre-encapsulated in N-containing organic linkers.[18–20] The process is similar to the pyrolysis of the mixtures containing metal, nitrogen and carbon atoms from metal doped polymers and carbon materials. However, these strategies are restricted to preparing anchored metal atoms on carbon and nitrogen carriers of undefined and impure support structure. Although a variety of SACs have been synthesized by these aforementioned methods, the SACs generally suffer from low TM metal loading, or/and inhomogeneous coordination environment.

There are some studies in literature reporting routes for the synthesis of high loading SACs.[21-24] Among them, the loading of SA can reach up to 20 wt%.[21] However, many were unstable against aggregation under the conditions, not well characterised, no clear established molecular interactions in their complex systems and were unable to differentiate the roles of single atoms from clusters in catalysis when the loading is high.[24] It is essential to formulate a reliable synthesis strategy to transfer the target-single atom-containing species to the substrate and effectively anchor the single atoms with high concentration.[25]

Recently, two-dimensional (2D) layered transition metal chalcogenides (TMCs) have been explored for many petrochemical conversions in the presence of chalcogens and for energy applications, including solar cells, batteries, light-emitting diodes, photocatalysts, electrocatalysts, thermoelectric generators due to their unique physicochemical properties.[26–32] These layered 2D materials are particularly studied as efficient catalysts for the production of hydrogen, which has been proposed as the ideal energy carrier by virtue of its highest gravimetric energy density with zero emission of carbon dioxide.[27] As a result, developing a common method to prepare high-loading of SAs supported on TMCs is highly desirable. Manipulating the basal plane of the TMC crystal surface by introducing surface defect sites promises to accommodate transition metal atom(s) in substantial amounts, desirable for improved catalytic activity.

In this study, we demonstrate the fabrication of highly stable, atomically dispersed TM catalysts on ultrathin 2D TMC materials (MoS_2, $MoSe_2$, WS_2 and WSe_2) with a loading of up to 10 wt% by synthesis using thiourea coordinated TMs as precursors. The TMC materials were first exfoliated into single molecular layers with high density anion vacancies by n-BuLi treatment in solution. These anion vacancy sites offered a coordination point for thiourea-TM complex, leading to a high density of SAs with strong TM-support interaction. This is applicable to a library of TMs including noble and non-noble TMs (Fe, Co, Ni, Cu, Pt, Ru, etc).

Fe SAs and clusters supported on single layered MoS_2 ($sMoS_2$) are demonstrated as model systems to correlate loading with catalytic performance. The Fe SA (Fe_1) can be atomically dispersed on $sMoS_2$ surface up to 10 wt%.When the loading is further increased, the Fe atoms begin to form clusters starting from surface Fe atoms pairs (Fe_2). These $Fe_1/sMoS_2$ and $Fe_x/sMoS_2$ exhibited excellent catalytic activity and selectivity for the reversed water gas shift reaction of CO_2 with good stability. We have used a wide variety of characterisation methods to understand the structural, compositional and chemical environment of the catalysts and to correlate their activity with structure.

RESULTS AND DISCUSSION

Preparation and Structural Characterization of TM-SACs. Figure 1a demonstrates the fabrication of SACs using Fe_1/MoS_2 with a theoretical loading of 10 wt% as an example. Single molecular layered MoS_2 ($sMoS_2$) was prepared by following our previously reported exfoliation method using n-BuLi intercalation.[28] The exfoliation creates a number of sulfur (S) vacancies, allowing the assembly of TM-thiourea complexes through self-nucleation under hydrothermal conditions. The as-obtained hybrid was further reduced at 300 ºC in diluted H_2 which resulted in Fe SAC supported on 2D MoS_2 (Fe-$sMoS_2$).

As seen in Figure 1b, bulk MoS_2 ($bMoS_2$) shows characteristic peaks in the X-ray diffraction (XRD) pattern, whereas these peaks diminish in the case of $sMoS_2$ and Fe-$sMoS_2$. This an indication of successful exfoliation of the layered structure which is further supported by atomic force microscopy (AFM) (Figure S1). The existence of S vacancies was verified by electron paramagnetic resonance (EPR), which is a sensitive technique to probe unpaired electrons. In comparison to $bMoS_2$, $sMoS_2$ shows a prominent signal at g = 2.005 (Figure 1c) corresponding to the unpaired electrons trapped at sulfur vacancies.[32] However, with the introduction of the Fe-thiourea complex ($Fe(thiourea)_4X_2$ where X= Cl or Ac), the intensity of this signal drops significantly, indicating that the Fe-thiourea complex refilled most of the electron density at the surface S vacancy sites of $sMoS_2$ during the hydrothermal process prior to further treatment. Previous studies also confirm that defective S vacancy sites possess high molecular affinity, especially for thiol-based molecules.[28–32] Thus, the S in one of the four thiourea ligands may occupy the S vacancy and coordinate to Mo. It is also possible that Fe itself may be placed at the S vacancy as a substituted site. However, our studies[28] indicated that single transition metal atoms preferentially occupy Mo top sites rather than S sites. In order to confirm that the atomic species on top of Mo sites are Fe atoms, Aberration-corrected high-angle annular dark-field scanning transmission electron microscopy electron energy loss spectra (AC HAADF-STEM-EELS) and synchrotron-radiation X-ray absorption fine structure (XAFS) analyses were used. Figures 1d, 1e and S2 show that Fe is present as single atoms, despite the high Fe loading (9.34 wt% from inductively coupled plasma -mass spectroscopy and optical emission spectroscopy (ICP-MS and -OES), Table S1) and the Fe adatoms are present on top of Mo sites in the 2D MoS_2 structure, presumably arising from refilling of the thiol tethered Fe complex to the neighbouring vacancies. Following. heat treatment, the higher contrast feature at the Mo site position corresponds to Fe from EELS, showing the characteristic signals of Fe *L3* and Fe *L2* edges at 708 and 721 eV, respectively.[33] The SA property of Fe-MoS_2 was further confirmed by extended X-ray absorption fine structure (EXAFS), as shown in Figure 1e. There is only a single peak at 1.77 Å attributed to the first Fe-S coordination shell in the

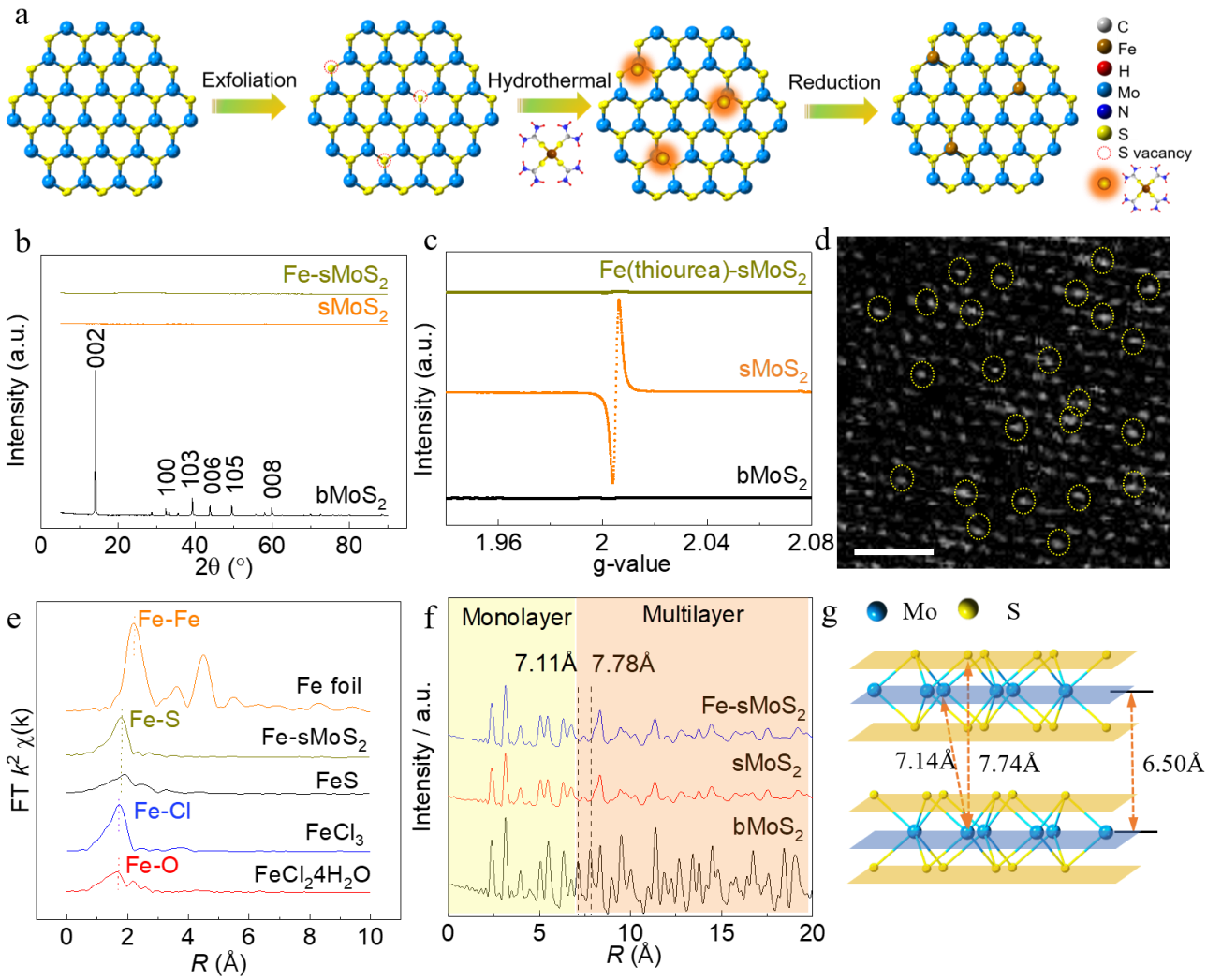

Figure 1. Preparation and structural characterization of 10%Fe-sMoS$_2$. **a.** Schematic illustration of the preparation of SACs. **b.** XRD and **c.** EPR spectra of bMoS$_2$, sMoS$_2$ and Fe-sMoS$_2$. **d.** ADF STEM image of Fe-sMoS$_2$ with single Fe atoms marked. Scale bar, 2 nm. **e.** k^3-weighted *R*-space Fourier transform spectra of EXAFS for Fe-sMoS$_2$, FeS, FeCl$_3$, FeCl$_2$4H$_2$O and Fe foil. **f.** PDF spectra of bMoS$_2$, sMoS$_2$ and 3%Fe-sMoS$_2$. **g.** A model of MoS$_2$ bilayer where each layer contains alternating S-Mo-S sub-layers/sub-columns.

as-reduced Fe-sMoS$_2$. Although there are some Fe atoms infrequently observed in pairs in Figure 1d, no Fe-Fe bonding at 2.22 Å was found in the EXAFS, indicating that only traces of Fe may be in clusters/pairs. In addition, the absorption edge of Fe-sMoS$_2$ from the X-ray absorption near edge structure (XANES) analysis in Figure S3 is similar to that of FeS indicating an average oxidation state between Fe^0 and Fe^{III}, which suggests a similar bonding environment and chemical status of Fe in Fe-sMoS$_2$ and FeS.

For sMoS$_2$ and Fe-sMoS$_2$, the bulk structure is disordered due to the exfoliated layers. Hence, using the Bragg peaks is limited for characterising the framework as no significant peaks were observed, as shown in Figure 1b. In contrast, pair distribution function (PDF) is a powerful tool for structural characterisation of materials with significant intrinsic disorder.[34,35] This technique uses both the Bragg and the diffuse diffraction component to yield structure parameters reflecting both the local structural disorder and the long-range order. The PDF spectra of dried bMoS$_2$, sMoS$_2$ and Fe-sMoS$_2$ are shown in Figures 1f and S4 together with a model of two-layer MoS$_2$, shown in Figure 1g. The sMoS$_2$ and Fe-sMoS$_2$ show attenuated PDF signals from 7 Å to 20 Å, the distance corresponding to 1 to 3 layers of sMoS$_2$, compared to bMoS$_2$. In the signal range larger than 20 Å, the signal significantly decays. Of particular interest, the signals at 7.11 Å and 7.78 Å, corresponding to Mo-Mo and Mo-S bonds respectively, in two layer MoS$_2$ (Figure 1g) are absent. This indicates that MoS$_2$ was exfoliated into single layers and that disordered restacking is within 2-3 layers during drying and reduction. To identify the local structure, the first-shell spectra in the range corresponding to to Mo-S, Mo-Mo and Mo-S bonds at 2.41 Å, 3.16 Å, and 3.99 Å respectively, were simulated (Figure S4) with errors within 2%. Simulated PDF patterns of Fe-sMoS$_2$ (Figure S4d), using a DFT model where Fe SA is

located on top of the Mo site (Figure S4f), fits well with the experimental data of PDF, indicating that the introduction of Fe SA did not cause further restacking of $sMoS_2$ and that the ultrathin layered framework was kept intact.

In order to synthesise SACs with high metal loading, we followed a 3-steage strategy. Initially, $bMoS_2$ was exfoliated to form monolayers with S vacancies and PVP was introduced in the colloidal solution to prevent restacking of the layers. Subsequently Fe-thiourea complex was used under hydrothermal conditions to refill the S vacancies within three-sublayers of S-Mo-S in a trigonal prismatic 2-H structure of mono-layer MoS_2 through thiol-terminated ligands.[30-32] Finally, the thermal treatment of the resultant solid yielded single atom Fe, located on top of Mo site, catalyst. To reveal the roles of PVP and thiourea, two control experiments were designed where Fe-$sMoS_2$ catalysts were synthesized by following the same experimental procedure but without the use of thiourea or Polyvinylpyrrolidone (PVP). These samples were examined by XAS. EXAFS spectra as shown in Figure S5, which show a new peak attributed to an Fe-Fe bond at 2.64 Å for the two controlled samples in additional to the Fe-S bond, belonging to Fe. Thus, maintaining the monolayer structure during synthesis with a high density of S vacancies is a prerequisite for the synthesis of high loading SACs. In the absence of thiourea and PVP, $sMoS_2$ is unable to support a high loading (ca. 10 wt%) of Fe SAs with the majority of Fe remaining atomically dispersed. To ensure the full utilization of SAs for catalytic reactions, the catalyst precursor was washed several times and calcined at 300 ºC under 5%H_2/N_2 to remove the surface organics that may cover the Fe atoms should be removed. The thermal gravimetric analysis (TGA) under nitrogen confirmed the total removal of organic species introduced during preparation. As shown in Figure S6, the curve of as-reduced Fe-$sMoS_2$ does not show any feature with no obvious weight loss, demonstrating the successful removal of thiourea and PVP by reduction and pre-treatments. To further confirm the absence of organic contaminants, IR spectroscopy (Figure S7) indicated that the signals of C-H and C-O vibrations derived from PVP were completely disappeared after reduction and no signal from thiourea was observed, demonstrating the catalyst surface was clean from organics.

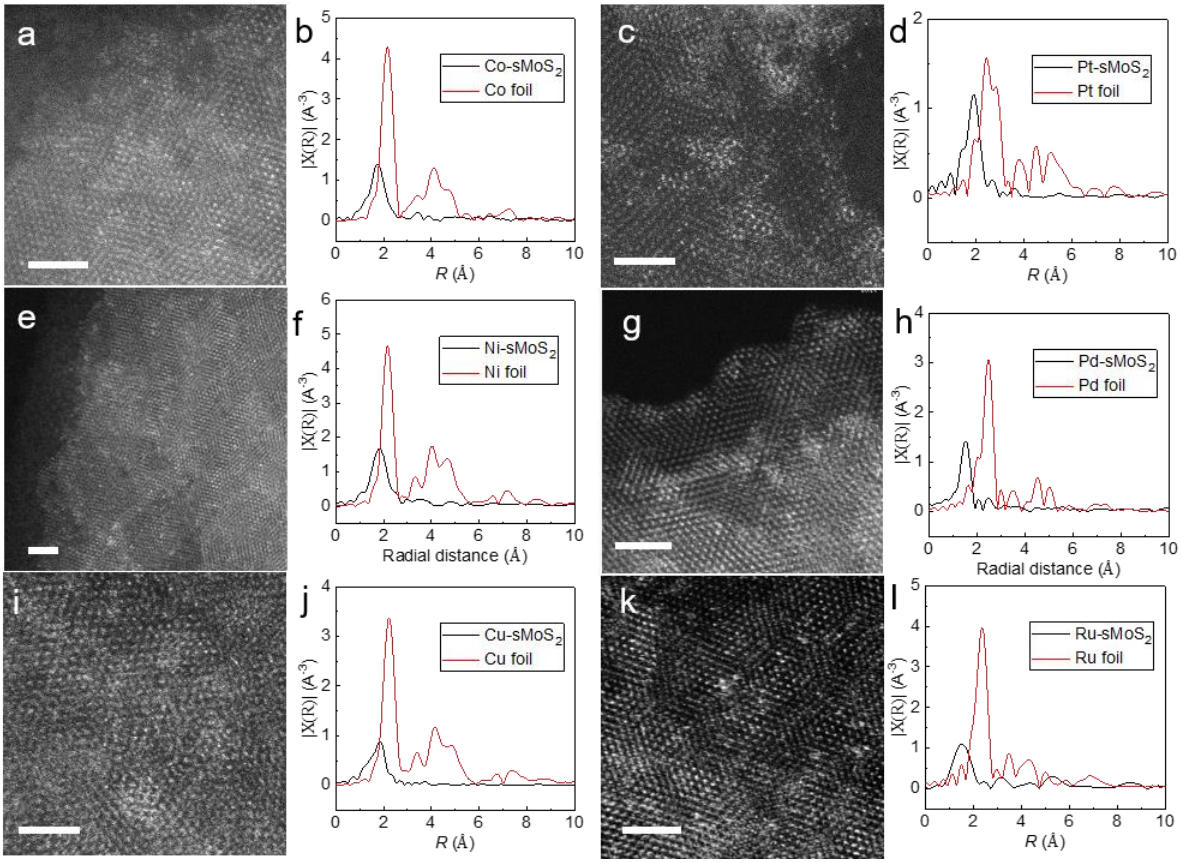

Figure 2. AC HAADF-STEM images (left) and EXAFS spectra (right) for TM-$sMoS_2$ and corresponding TM foils (10 wt%). **a, b.** Co. **c,d.** Pt. **e,f.** Ni. **g,h.** Pd. **i,j.** Cu. **k,l.** Ru. Scale bars, 2 nm in all cases.

The versatility of the synthesis. Thiourea strongly coordinates to a variety of TM ions[36], giving a route to extending our synthesis strategy to other TMs. We therefore prepared thiol complexes of non-noble (Co, Ni, Cu) and noble (Pt, Pd, Ru) TMs and used these in the synthesis of corresponding SACs with exfoliated 2D monolayer materials as the support. The metal loading was adjusted to 10 wt% in all as-prepared catalysts. XRD spectra and AC HAADF-STEM images were used to initially

identify the aggregation states of metal species and the texture of the catalysts. ICP-OES was used to measure the concentration of TM species which shows that most of the TM species from the TM precursors were successfully deposited onto the $sMoS_2$ during preparations (Table S1). XRD spectra shown in Figure S8 show no clear crystalline features from the corresponding TMs, indicative of a high dispersion of TMs on $sMoS_2$ even at a high metallic loading. AC HAADF-STEM images (Figures 2a,c,e,g,i,k) show that these TM species are also atomically dispersed over $sMoS_2$ rather than forming TM nanoparticles. EXAFS spectroscopy is sensitive to the local environment of metal atoms and was thus used to confirm the presence of SAs in the various TM-SACs. Figures 2b,d,f,h,j,l show k^3-weighted *R*-space Fourier transform spectra of EXAFS for the SACs along with relevant reference metal foils. For each TM-SAC, the spectrum was distinct from that of the relevant TM foil. All the SACs contain a single peak in the first shell in *R* space at around 1.80 Å. This distance is shorter than the typical TM-TM bond distance as indicated by the red line corresponding to the TM foil (Figure 2). These results clearly demonstrate that the TM species are atomically dispersed on the $sMoS_2$, which is consistent with the XRD and AC HAADF-STEM results. Furthermore, we expanded the synthesis method using other exfoliated 2D materials ($MoSe_2$, WS_2, WSe_2) as supports for SACs. AC HAADF-STEM results (Figure S9) show that Pd SAs were successfully anchored onto these ultrathin 2D materials, demonstrating that the synthesis method is applicable to a wide range of different TMs and 2D materials.

Notice that our current synthetic method relies on usage of thiourea and butyllithium to prepare metal complexes and exfoliated single MoS_2 layer before their immobilization reactions, which may be cumbersome, expensive and not green in practice. We thus tried to modify this synthetic method without using thiourea and butyllithium (Figure 5b). For example, MoS_2 was exfoliated by hydrazine instead of using butyllithium[28] and iron acetate was used. Only single characteristic peak is observed for 3%Fe-MoS_2 but two peaks in 10%Fe-MoS_2 indicate the Fe aggregation at the high loading. Fe SAC the modified method is thus applicable when the loading is 3 wt%, indicating the single atom catalyst can also be prepared by using simple water soluble Fe salt (see SI).

Structural evolution with progressive Fe introduction. One benefit of the strategy of creating and refilling surface anion vacancy sites is that the defined structure from SA to clusters can be controlled and monitored progressively with atomic precision, to gain fundamental insights on the active site and the effect of progressive structural evolutions. Fe-$sMoS_2$ was used as an example to study the structural evolution by varying the Fe loading.

Progressive introduction of Fe from 3 to 20 wt% on $sMoS_2$ was monitored using different characterisation methods. The ICP-OES results in Table S2 show that the deviation of the actual loadings of Fe from the theoretical ones is small, indicating successful stoichiometric loading of Fe. X-ray photoelectron spectroscopy (XPS) was used to study the chemical composition and electronic structure on the surface of these samples.[37] It is noted that the calculated surface composition from XPS is very close to the bulk composition obtained from ICP-OES (Table S2) which signifies that most of MoS_2 retained a monolayer structure during Fe deposition, leading to homogeneous Fe dispersion on the surface support.

The Fe dispersion was then studied using XRD, EXAFS, and AC HAADF-STEM. XRD spectra (Figure S10) show no crystalline Fe signals, indicating high dispersion even at 20 wt% of Fe. A peak at 15° is attributed to the vertical plane of MoS_2 (002), due to from restacking of layers during Fe deposition and solvent evaporation. Intriguingly, the intensity of this peak gradually decreases as the loading of Fe increases suggesting that the accommodation of Fe atoms on MoS_2 nanosheets can lower the degree of restacking during drying. The k^3-weighted *R*-space Fourier transform spectra from EXAFS (Figure 3a) indicate a single Fe-S coordination at 1.80 Å, thus providing evidence of single atom dispersion, up to 10 wt% of Fe loading. However, increasing the Fe loading to 15 wt% or 20 wt% results in the emergence of new features at 2.57 Å, assigned to a Fe-Fe coordination shell. The Fe-Fe bonding distance in Fe-$sMoS_2$ is longer than that in Fe foil (2.22 Å), which may be due to scattering between neighbouring Fe atoms on two top Mo sites. AC HAADF-STEM images (Figure S11) show a gradual increase in the density of Fe SAs with the progressive addition of Fe species. Most Fe SAs are isolated for Fe loadings less than 10 wt%. However, for Fe loading at 15 wt% and 20 wt%, some of the Fe atoms form small lamellar 2D clusters rather than aggregating into 3D nanoparticles consistent with a longer Fe-Fe bond distance compared to that in Fe foil.

The chemical status of Fe can be analysed based on the energy of the edge and pre-edge features in XANES spectra (Figures S12 and 3b).[38] The edge of all the Fe-$sMoS_2$ catalysts falls between that of Fe foil and Fe(III), indicating that the valence is between Fe(0) and Fe(III). As the Fe coordination geometry affects both the shape and intensity of the pre-edge peak, the pre-edge region can be used to obtain quantitative information on the oxidation state and local environment of the Fe species. It is noted that the pre-edge of Fe-$sMoS_2$ at 10 wt% Fe loading at 7112.8 eV is at the same position as in hydrated $FeCl_2$ and FeS, indicating that Fe SAs are in the Fe(II) oxidation state. Upon increasing the Fe loading, the Fe pre-edge energy is shifted by 0.69 eV ($\Delta1$) and 0.90 eV ($\Delta1+\Delta2$) for the 15 wt% and 20 wt% Fe-$sMoS_2$ samples, respectively. This indicated that some of the Fe atoms are in Fe(III) oxidation state in these samples where Fe lamellar cluster formation is observed. In order to understand how the chemical state of Fe changes on Fe-Fe bond formation, we constructed (2×2) supercell models of 2H-MoS_2 with a single Fe atom (Fe_1), a 2-Fe atom cluster (Fe_2) and a 3-Fe atom cluster (Fe_3) located on top of Mo sites to simulate XANES spectra of these models. The simulations are shown in Figure 3c. In agreement with the experimental data, the pre-edges of both simulated Fe_2-$sMoS_2$ and Fe_3-$sMoS_2$ shift to higher energies, implying that the formation of Fe clusters could cause an energy shift higher positive values. The calculated energy shift of Fe_2-$sMoS_2$ (0.65 eV ($\Delta3$)) compared to Fe_1-$sMoS_2$ is very close to the energy shift (0.69 eV ($\Delta1$)) observed for 15%Fe-$sMoS_2$ relative to 10%Fe-$sMoS_2$, in which Fe is in the form of single atoms only. This strongly suggests that most of Fe atoms are present as Fe-Fe pairs in 15%Fe-$sMoS_2$. As the energy shift in the case of 20%Fe-$sMoS_2$ (0.90 eV ($\Delta1+\Delta2$)) is smaller

than the ones simulated for Fe_3-$sMoS_2$ (1.37 eV ($\Delta3+\Delta4$)), we propose that Fe is in a mixed environment where both Fe_2 and Fe_3 clusters are present. These arguments are further supported by performing detailed EXAFS and Wavelet analyses[36]. The wavelet transformation for the Fe k-edge EXAFS signals are shown in Figure 3d-i. For Fe foil, there are two hotspots at 8.4 $Å^{-1}$ (k value) with R values of 2.22 Å and 4.45 Å. These are attributed to the Fe-Fe scattering in the first and second shells. However, only one hotspot region at 1.8 Å is observed for Fe-$sMoS_2$ samples with Fe loadings between 3-10 wt%, indicative of atomic dispersion of Fe species and this hotspot is likely to be caused by Fe-S scattering from the first shell. However, the hotspot splits into three in the first shell when the Fe loading is increased to 15 wt% and 20 wt%. Two

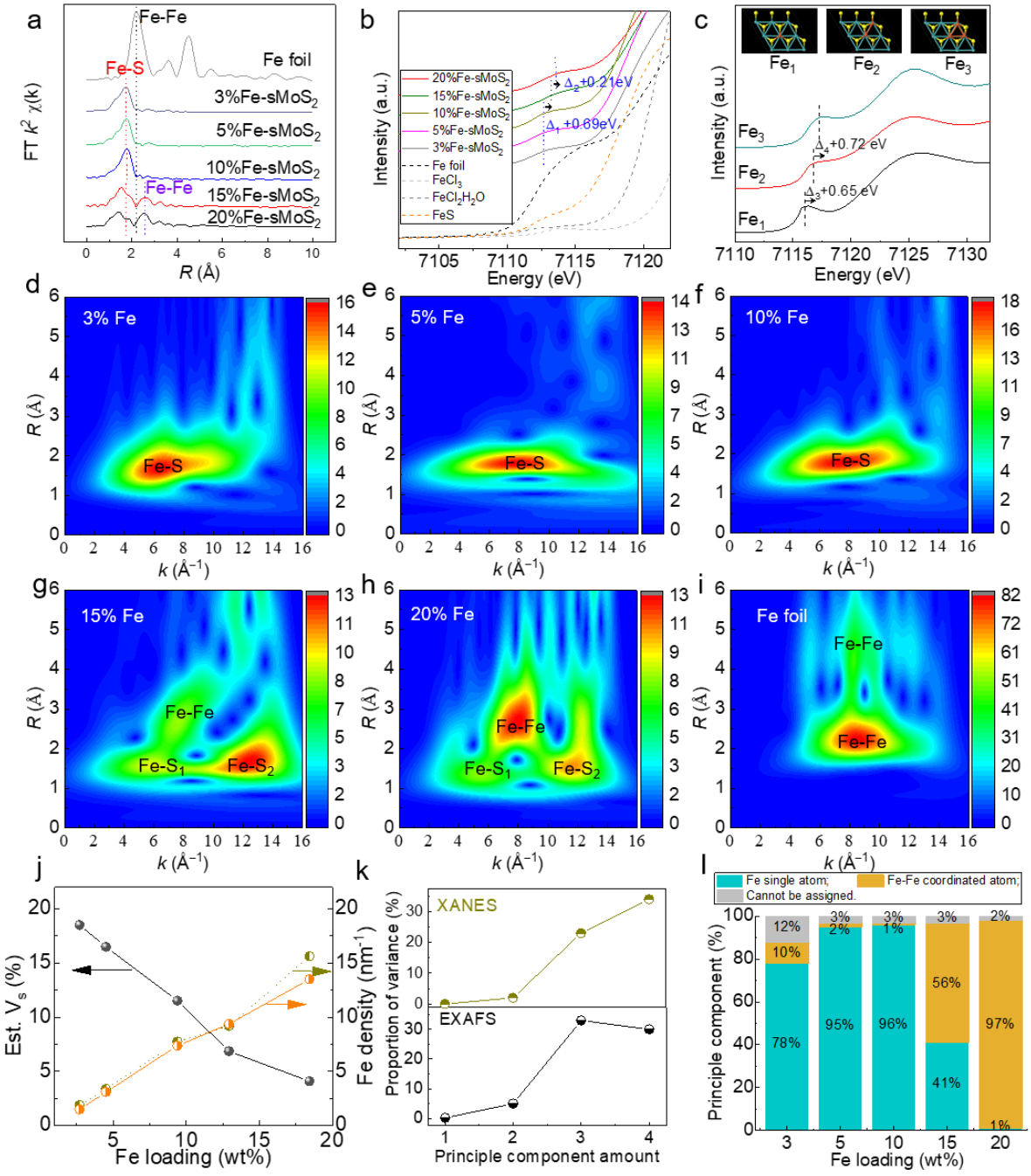

Figure 3. Structural evolution of Fe-$sMoS_2$ with progressive additions of Fe with weight loading from 3% to 20%. **a.** k^3-weighted *R*-space Fourier transform spectra of EXAFS and **b.** Pre-edge of Fe *k* -edge XANES spectra for Fe-$sMoS_2$. FeS, $FeCl_3$, $FeCl_24H_2O$ and Fe foil were used as references. **c.** Simulated Fe *k* -edge XANES spectra for Fe_1, Fe_2, and Fe_3 clusters supported on $sMoS_2$, **d-i.** Wavelet transformation for the Fe *k*-edge XAFS

signals of Fe-sMoS$_2$ and Fe foil based on Morlet wavelets with optimum resolutions at the first and higher coordination shells. Intensity decreases in the order of red, yellow, green, and blue. **j.** Estimated vacancy concentration (Est. Vs, black solid line) and Fe density obtained from the loading (mustard dashed line) and statistical calculations from STEM images (orange solid line). **k.** Proportion of variance for 1-4 principle component species for XANES and EXAFS data based on the F-test. **l.** Principle component as a function of Fe loading.

hotspot regions at around 1.80 Å (R-value) are assigned to Fe-S scattering while the third hotspot located at 2.8 Å (R-value) is due to Fe-Fe scattering. Notably, the Fe-Fe scattering is enhanced with higher Fe loading in 20%Fe-sMoS$_2$. These results strongly suggest that Fe clusters are formed in the 15%Fe-sMoS$_2$ and 20%Fe-sMoS$_2$ samples. On the basis of wavelet analyses, all the EXAFS spectra of Fe-sMoS$_2$ were fitted and the results are shown in Figure S13 and Table S3. The R factors were all within 1.5% to ensure the accuracy of the fitting. For the Fe content of 10 wt%, only Fe-S scattering with a coordination number (CN) of *ca.* 3 could be fitted. Additional Fe-Fe scattering was found for 15%Fe-sMoS$_2$ and 20%Fe-sMoS$_2$, with a CN of 1.25 and 2.18 respectively, which suggest the formation of few atom clusters of Fe in these samples. It is also noted that all the Fe-sMoS$_2$ catalysts show a Fe-S scattering with a CN of *ca.* 3, meaning that each Fe atom is supported by three S atoms and the Fe atoms in clusters are deposited on the same layer in a coplanar manner, which agrees with our observations from STEM images.

Furthermore, first principle DFT was employed to monitor the structural evolution with progressive Fe introduction of Fe_1, Fe_2 and Fe_3 into sMoS$_2$. The three optimised models shown in Figure S14 indicate that each Fe atom is preferentially located on a top Mo site and coordinated to three S atoms. The Fe_1-sMoS$_2$ has the same bonding distance for three Fe-S bonds, which is consistent with our experimental results. For Fe clusters, our model suggests that Fe atoms sit preferentially at the neighbouring top Mo sites, causing elongation of the Fe-Fe bond distance compared to that in Fe foil. In addition, the distance of the Fe-S bonds slightly deviate from each other, as implied in the EXAFS fitting (Table S3). All these experimental and calculated results support that our hypothesis that progressive introduction of Fe induces a structural evolution from Fe SACs to few atom clustered Fe.

Mo k edge XAS spectra have been conducted to investigate the environment change of Mo during the preparation procedure. As shown in Figure S15a, there is no new peak emerged after exfoliation of bMoS$_2$ or Fe loading to sMoS$_2$. Thus, no Fe-Mo bonding can be inferred with no direct bonding interaction between Fe and Mo. Notice that the two major peaks are arisen from Mo-S scattering, which significantly decrease after the exfoliation of bMoS$_2$ due to the formation of S vacancies. However, the peak intensity only slightly recovers even after the introduction of excess Fe thio-complex with the anticipated total refilling of the S vacancies. In Mo k edge XANES spectra (Figure S15b), the edge region analysis shows that Mo k edge shifts towards lower energy as the exfoliation of MoS$_2$ but shifts a little back when Fe thio-complex is doped. This indicates that Mo becomes more electron richer as the formation of S vacancies after exfoliation but can slightly return to the direction of the original value upon the Fe thio-complex introduction. Similar conclusion can be made based on the absorption analysis of 1s→5p dipole-allowed electronic transition. The absorption is much weakened when MoS$_2$ is exfoliated but can slightly return after the Fe thio-complex introduction. XPS spectra of Mo3d and S2s have been investigated (Figure S16). It is interesting to find that with the introduction of Fe, both the peaks of Mo3d and S2s shift towards higher binding energy, indicative of the electronic donation from Mo and S to Fe, consistent with the result of XANES spectra. Thus, the S vacancies can enrich electron density of Mo but it cannot return to the original value by refilling the vacancies due to the strong electron donating to the Fe atoms by the sMoS$_2$ structure.

XPS data (Figures S17 and S18) was also used to examine the amount of surface species and the oxidation state of Fe. The Fe2p signal is enhanced as the Fe loading increases, suggesting more surface Fe species are anchored on sMoS$_2$. An. S. et al. found that ultra-small clusters and single-atom Fe sites embedded in graphitic carbon nitride (g-C_3N_4) have a Fe2p$_{3/2}$ peak at a relative high binding energy (~710.5 eV) as Fe(II).[24] It was also reported that Fe2p$_{3/2}$ of Zn[Fe(CN)$_5$NO] appears at 710.2 eV.[39] Therefore, Fe2p$_{3/2}$ peak in Fe-sMoS$_2$ is deconvoluted into two peaks at 710.5 eV and 712.4 eV, attributing to Fe(II) and Fe(III), respectively. The main specie is Fe(II), which is consistent with the Fe k edge XANES study in Figure 3b. Further increasing the Fe loading led to the increment of Fe(III) species as well as Fe(II)[40] supporting the observations made from EXAFS. The amount of S vacancies (Vs) was estimated based on the ratio of S and Mo from XPS.[41] The amount of Vs decreases linearly with Fe loading (Figure 3j and Table S4). The Fe density was then calculated based on the ICP results and STEM images. The deviation is minor, consistent with successful loading of high concentration of Fe atoms with a coplanar structure. Principal component analysis (PCA) was then used to extract chemical information, improving our understanding of chemical and physical material properties for complex systems.[42] In this work, PCA from EXAFS and XANES (Figure 3k) indicates that there are 1 or 2 Fe species in the Fe-sMoS$_2$ as the proportion of variance explained within 5% based on the Fischer (F) test. The Fe content in the five samples are thus monitored for Fe single atom, Fe cluster and unassigned species. As shown in Figure 3l, the main component in these samples is Fe single atom at loadings below 10 wt%. However, increasing the loading of Fe generates Fe clusters, which consistent with EXAFS fitting.

Catalytic performance for reverse water gas shift (RWGS). CO_2 is the most widely known global greenhouse gas, and recently, much attention has been paid to CO_2 capture and utilisation. In particular, synthesis of valuable chemicals and fuels, such as methanol, from CO_2 has been of great interest. In industry, methanol is produced via the CAMERE process[43] which involves the formation of CO via reverse water gas shift (RWGS)[44] followed by methanol synthesis using a gas mixture of

CO_2/CO/H_2. RWGS reaction is a very important pre-reaction especially regarding to the recent use of renewable hydrogen to reduce CO_2 to CO both thermal and electrochemically before a mixture of CO/CO_2 is used for later fast methanol synthesis. However, chemical reactions using CO_2 as reactants are generally highly endothermic with unfavourable equilibrium positions towards product(s) and hence generally require elevated operating temperatures. For instance, for RWGS, the typical reaction temperature is above 500 °C.[45] Since RWGS is one of the key processes in carbon dioxide hydrogenation to form methanol, great efforts have been devoted to prepare novel catalysts that are active and selective under mild operating conditions. There is also a considerably interest in developing sulphur tolerant RWGS chalcogenide based catalysts.

Despite the fact that SACs are likely to show high intrinsic activity for CO_2 hydrogenation per single metal atom site, the catalytic activity per gram or unit packed volume might be low due to their low TM loadings. On the other hand, SACs can achieve maximum atom utilisation. Therefore, maximizing the loading of SAs can optimize the catalytic performance and improve the practical economic viability of catalytic systems. Having illustrated the structural evolutions of Fe-sMoS_2 catalysts with different loadings, we compared their catalytic performances in CO_2 hydrogenation. The dominant product over Fe-sMoS_2 was CO with a selectivity of 99.9% at ambient pressure (Figure 4a). Increasing the pressure to 10 bar led to the formation of CH_4 as the main by-product for all catalysts (Figures S19 and S20) while trace amounts (<1%) of C_2 and C_3 hydrocarbons and methanol were also observed when the Fe loading was increased above 10 wt%. These results indicate that Fe SA or small coplanar Fe clusters are not able to couple C species to form higher carbon chains due to their highly dispersed nature on the TMC monolayer surface. Increasing the reaction temperature resulted in higher CO_2 conversion for all catalysts until 350 °C, after which the conversion levelled off. Among Fe-sMoS_2 with various Fe loading, 10%Fe-sMoS_2 showed the best catalytic activity with a CO selectivity of >98% even at elevated pressure and temperature (Table 1 and Figures S19, S20). As shown in Table 1, 10%Fe-sMoS_2 with maximum Fe SAs shows superior performance than most of the reported Fe based catalysts at a lower operating temperature.

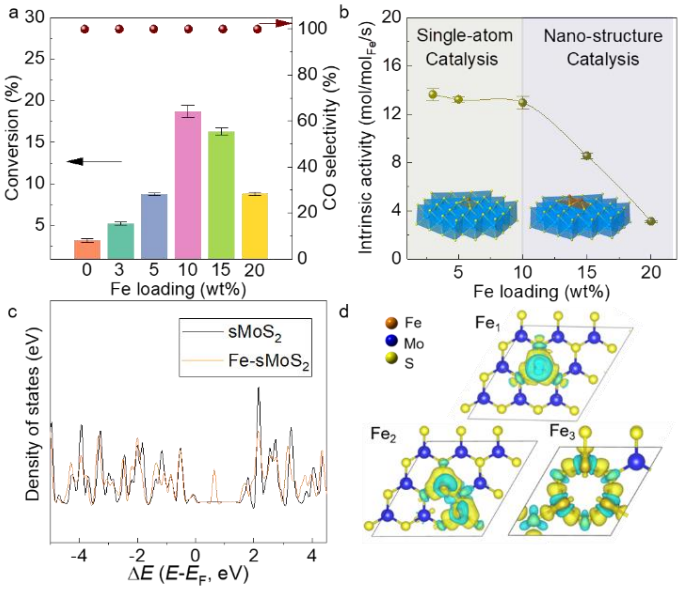

Figure 4. Catalytic performance for RWGS over Fe-sMoS_2 and bulk MoS_2. **a.** Conversion of CO_2 and selectivity of CO in RWGS. **b.** Intrinsic activity over Fe-sMoS_2 as a function of Fe loading. **c.** Calculated density of states of sMoS_2 and Fe-sMoS_2. **d.** Charge differences of Fe-sMoS_2 and sMoS_2. Condition: 1 bar, 300 °C, gas hourly space velocity (GHSV), 9000 mL/g/h.

Bulk MoS_2 presented an extremely low CO_2 conversion of around 3%. However, incorporating Fe species onto sMoS_2 led to a considerable increase in the CO_2 conversion to CO. The conversion of CO_2 increased linearly as the Fe loading increased from 3 wt% to 10 wt%, as shown in Figures 4a and S19. This is understandable as the atomic density of Fe SAs increases with loading. The conversion of CO_2 was found to be 17.2% with a high selectivity of 99.9% to CO. However, further increasing the loading to 15 wt% and 20 wt% resulted in inferior catalytic performance. This demonstrates that the formation of Fe clusters is detrimental to the activation of CO_2.

To express the intrinsic activity per metal it is common to derive the value from metal dispersion generally using CO or H_2 chemisorption for supported metal catalysts. However, this is prerequisite that the support would not interfere the CO/H_2 chemisorption on metal surface. Single molecular 2H or 1T MoS_2 structure is not an inert support but akin to semiconductive /metallic surface towards strong adsorption/migration of these gaseous species.[28] As a result, the estimation of dispersion cannot simply be conducted by the conventional means. It is possible that the coverage by organic species during preparation and the restacking could reduce the amount exposed Fe species, limiting the full utilization of Fe atoms. However, TGA and IR in Figures S6 and S7 confirm the successfully removal of these organic species including thiourea and PVP. Although there is a small peak at 14.4° attributable to (002) stacking in c direction with the interlayer spacing of 6.5 Å, according to PDF the 2 to 3 layer are in fact stacked in highly disordered manner to each other (the signals at 7.11 Å and 7.78 Å, corre-

sponding to Mo-Mo and Mo-S bonds, respectively, in two layers of MoS_2 are completely disappeared, see Figure 1g). As a result, the large spatial distances between the randomly/disordered stacked individual layers decorated with Fe atoms do not seem to strongly restrict the access of small substrate molecules (H_2/CO_2). However, it is rather difficult to experimentally prove the fully accessibility of Fe sites using chemisorption technique (CO or H_2) due to their weak adsorption in the presence of active single molecular layer MoS_2. Therefore, the 'intrinsic activity' was calculated based on the total Fe loading with the assumption of Fe is fully dispersed with no inaccessible Fe species embedded in the layer re-stacking. Thus, the intrinsic activity is simply calculated based on the actual Fe loading and the results are plotted as a function of Fe loading in Figure 4b. Interestingly, the intrinsic activity was constant for the Fe loadings less than 10 wt%, and the activity attenuated dramatically in a linear fashion as more Fe species were introduced. Combined with our structural analysis, we conclude that Fe SA is the active site for CO_2 hydrogenation to CO and the increase in surface density of Fe SA sites would induce the formation of Fe clusters, lowering the intrinsic catalytic activity. The formation of coplanar Fe clusters clearly causes a decrease in the electron density of an Fe atom as the Fe spectra are significantly shifted to higher binding values as indicated by XANES and XPS spectra. To confirm this the effect of Fe loading on the electronic structure was evaluated based on the calculated density of states in $sMoS_2$ and Fe-$sMoS_2$ (Figure 4c). Addition of a single Fe atom led to a change in the electron density of MoS_2, further illustrating the interaction between Fe and MoS_2. Notably, new energy states at the conduction band 0.73 eV above the Fermi level emerged for Fe-$sMoS_2$, derived from a Fe 3d orbital. Therefore, the Fe atom acts as an electron mediating site to activate substrates and the electron difference between Fe-$sMoS_2$ and $sMoS_2$ is shown in Figure 4d. Fe SA gives the highest electron density while the formation of Fe clusters leads to a reduction in electron density per Fe atom. These results closely match the XPS results shown in Figure S17. Combined with the measured catalytic performance, this clearly demonstrates that Fe SA is the active site for RWGS and the formation of Fe cluster(s) is detrimental to this activity. The high electron density of Fe is anticipated to make the binding of substrates stronger due to electron back donation hence leading to higher activity. CO_2-temperature program desorption (CO_2-TPD) was further performed to confirm this. As indicated in Figure 5a, $sMoS_2$ shows a small peak at 520 ^oC, which corresponds to the adsorption of CO_2 at S vacancies.[52] In comparison, the signal dramatically increased after Fe was doped onto $sMoS_2$. The main peak emerged at 720 ^oC is attributed to the adsorption of CO_2 on Fe species. 10%Fe-$sMoS_2$ with utmost Fe single atoms shows the highest capacity for CO_2 adsorption/activation. 15% and 20%Fe-$sMoS_2$ show lower peak size, indicating the formation of Fe clusters does not facilitate the CO_2 adsorption/activation. Accordingly, Fe single atom may give high electron density while the formation of Fe clusters leads to a reduction in electron density per Fe atom. Thus, the CO_2-TPD confirms that the Fe single atoms are more superior than Fe clusters for CO_2 binding/activation, which is also essential for RWGS reaction. Finally, the stability of Fe SACs was evaluated at 300 ^oC under CO_2/H_2 for a prolonged time. The 10%Fe-$sMoS_2$ shows essentially no decrease in catalytic conversion and selectivity for more than 500 h of testing time, as shown in Figures S21 and S22. Furthermore, no Fe-Fe scattering feature was found in EXAFS analysis (Figure S23), while the 10%Fe-$sMoS_2$ after reaction maintains a Fe-S coordination environment identical to that of the freshly prepared sample (Figure 1e). This long term stability of Fe-$sMoS_2$ with a high loading of Fe species is attributed to the strong coordination of three S atoms to each Fe atom arising from filling surface anion vacancy sites. These results suggested that SACs prepared

Table 1. Catalytic performance of Fe-$sMoS_2$ in RWGS reaction compared to state-of-the-art catalysts[a]

Catalyst	T (^oC)	GHSV (mL/g/h)	H_2:CO_2	Rate (μmol/g/s)	Selectivity (%)	Ref.
10%Fe-$sMoS_2$	300	27000	3	3.2	99.9	this work
10%Fe-$sMoS_2$	400	27000	3	8.1	99.9	this work
10%Fe-$sMoS_2$	500	27000	3	15.7	99.9	this work
Fe hematite nanosheet	510	12000	1	3.7	-	46
Fe_3C	480	45000	4	7.2	>99	47
Fe/CeO_2-Al_2O_3	500	30000	4	2.45	80	48
Fe/CeO_2	400	60000	4	6.4	100	49
Fe/Si-1	400	731	1	0.36	96.7	50

Fe oxide	600	6000	1	13	85	43
Pt-Al_2O_3	400	12000	1.4	1.6	-	51
Pd-La_2O_3/MWCNT	400	72000	3	~8.3	~100	52
Rh/S-1 [b]	300	3600	3	0.006	85.7	53

[a]1 bar. [b]10 bar.

Using this method active Fe containing catalyst (10%Fe/$sMoS_2$) for RWGS can be preliminary achieved without rapid deactivation as compared with typical supported Fe oxide in the presence of thiophene. This new but more sulfur tolerant RWGS catalyst under on stream reaction conditions may open up practical catalytic applications (Figure S24).

Diffuse reflectance infrared Fourier transform spectroscopy (DRIFTS) has been conducted to study the mechanism of CO_2 reduction. As presented in Figure 5b, CO is progressively generated when CO_2 and H_2 are continuously flowed through the 10%Fe-$sMoS_2$. However, no intermediates such as formate or formic species of strong IR sensitivity is actually detected. This supports to the fact that the catalytic CO_2 reduction may follow a direct CO_2 redox splitting mechanism to CO and O on Fe-$sMoS_2$ as similar to the related WGS mechanism by metal atoms on support claimed by a number of researchers in the literature.[53] In addition, by comparing the DRIFT spectra (Figure S25) at 30 min over $sMoS_2$ and 10%Fe-$sMoS_2$, the signal of CO over 10%Fe-$sMoS_2$ is significantly higher than that over $sMoS_2$, further confirming the promotion of Fe single atom for CO_2 reduction to CO.

A proposed reaction mechanism based on our DFT calculation is briefly summarised in Figure 5c. Upon exposure of H_2 to the edge sites of $sMoS_2$, dissociative of H_2 will take place, followed by the readily transfer of H to the neighbour terrace S sites of the metallic like $sMoS_2$ (1T and 2H) support. (an alternative model based on the initial H_2 activation on Fe site of $sMoS_2$ and then transferred to terrace S sites may also be feasible). These steps are energetically favourable due to the high affinity of H to terrace S site of $sMoS_2$. The H coverage on such support interface is generally known. Also, MoS_2 especially single layer MoS_2 is well accepted to be extremely active as support for transition metal(s) in hydrogen production from catalytic/photocatalytic/electrocatalytic water splitting due to involvement of H-S.[54] CO_2 (O=C=O) is then activated by Fe with a bent adsorption geometry indicative of the strong interaction of its terminal O by the neighbour H from the support. It then followed by its redox dissociation to CO and OH probably via a short lifetime of COOH (undetected by DRIFTS) and then H_2O from the catalyst surface. The described pathway depicts the strong support effect to the metal atom in catalysing the RWGS, which is in line with the DFT calculations of supported single metal atom on metallic like support surface from the literature.[55]

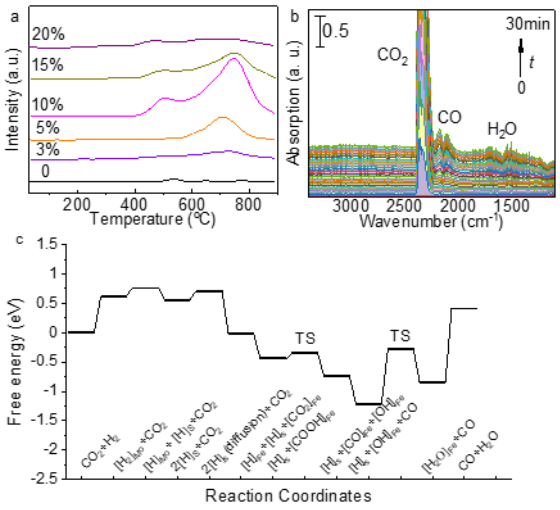

Figure 5. (a) CO_2-TPD over $sMoS_2$ with different Fe loadings. (b) Time dependent DRFTS spectra over 10%Fe-$sMoS_2$ at 300 °C under CO_2 and H_2 (1:3); (c) A proposed mechanism for RWGS on Fe-$sMoS_2$.

CONCLUSION

In summary, a new synthetic strategy of creating and refilling of vacancies on exfoliated 2D materials was developed to fabricate high loading of TM SACs on monolayer TMC supports. The method appears to be universal and can be used to prepare a library of TMs (Fe, Co, Ni, Cu, Pt, Pd, Ru and so on) on 2D materials via surface anions anchoring sites (MoS_2, $MoSe_2$, WS_2 and WSe_2). The layered structure covered with anions and a high density of surface vacancies are the two prerequisite conditions for the preparation of SACs at high loading. Therefore, exfoliation of 2D materials to form monolayers allowed a loading of SA-TMs up to 10 wt%. The atomic metal dispersion at such a high concentration is attributed to the strong metal-support interactions which are related to the high affinity of the chalcogenide anion to TMs due to strong soft acid base electronic interactions and the kinetic refilling of the surface anion vacancies with thio-ligands of TMs on doping, prior to heat treatment and reduction. We envisage that similar modified synthesis methods could also be applied other layered materials such as graphene, and layered double hydroxides. Using this method, well-defined catalytically active sites, with sizes ranging from SA to clusters, can deliberately be prepared

and used as model catalysts to study the kinetics and reaction mechanisms of various catalytic chemical processes.

ASSOCIATED CONTENT

Supporting Information. This material is available free of charge via the Internet at http://pubs.acs.org." Experimental details, nanomaterials characterization spectra and additional analysis are all included.

AUTHOR INFORMATION

Corresponding Author

* edman.tsang@chem.ox.ac.uk

ACKNOWLEDGMENT

The support of this project from the IUK-EPSRC of UK (DGE 102000) is gratefully acknowledged. The authors wish to thank AIST in Japan for EELS analysis and NSRRC in Taiwan for XAS facilities and Diamond Light Souce in UK for accessing STEM under University of Oxford and ePSIC consortium (EM20677).

REFERENCES

(1) Seh, Z. W.; Kibsgaard, J.; Dickens, C. F.; Chorkendorff, I.; Nørskov, J. K.; Jaramillo, T. F. Combining Theory and Experiment in Electrocatalysis: Insights into Materials Design. *Science* **2017**, *355*, 6321.

(2) Wang, A.; Li, J.; Zhang, T. Heterogeneous Single-Atom Catalysis. *Nat. Rev. Chem.* **2018**, *2* (6), 65–81.

(3) Chen, Y.; Huang, Z.; Ma, Z.; Chen, J.; Tang, X. Fabrication, Characterization, and Stability of Supported Single-Atom Catalysts. *Catal. Sci. Technol.* **2017**, *7* (19), 4250–4258.

(4) Zhang, H.; Liu, G.; Shi, L.; Ye, J. Single-Atom Catalysts: Emerging Multifunctional Materials in Heterogeneous Catalysis. *Adv. Energy Mater.* **2018**, *8* (1), 1701343.

(5) Su, X.; Yang, X.-F.; Huang, Y.; Liu, B.; Zhang, T. Single-Atom Catalysis toward Efficient CO_2 Conversion to CO and Formate Products. *Acc. Chem. Res.* **2019**, *52* (3), 656–664.

(6) Liu, P.; Zhao, Y.; Qin, R.; Mo, S.; Chen, G.; Gu, L.; Chevrier, D. M.; Zhang, P.; Guo, Q.; Zang, D.; Wu, B.; Fu, G.; Zheng, N. Photochemical Route for Synthesizing Atomically Dispersed Palladium Catalysts. *Science* **2016**, *352* (6287), 797–800.

(7) Corma, A.; Concepción, P.; Boronat, M.; Sabater, M. J.; Navas, J.; Yacaman, M. J.; Larios, E.; Posadas, A.; López-Quintela, M. A.; Buceta, D.; Mendoza, E.; Guilera, G.; Mayoral, A. Exceptional Oxidation Activity with Size-Controlled Supported Gold Clusters of Low Atomicity. *Nat. Chem.* **2013**, *5* (9), 775–781.

(8) Lang, R.; Xi, W.; Liu, J.-C.; Cui, Y.-T.; Li, T.; Lee, A. F.; Chen, F.; Chen, Y.; Li, L.; Li, L.; Lin, J.; Miao, S.; Liu, X.; Wang, A.-Q.; Wang, X.; Luo, J.; Qiao, B.; Li, J.; Zhang, T. Non Defect-Stabilized Thermally Stable Single-Atom Catalyst. *Nat. Commun.* **2019**, *10* (1), 234.

(9) Jones, J.; Xiong, H.; DeLaRiva, A. T.; Peterson, E. J.; Pham, H.; Challa, S. R.; Qi, G.; Oh, S.; Wiebenga, M. H.; Pereira Hernandez, X. I.; Wang, Y.; Datye, A. K. Thermally Stable Single-Atom Platinum-on-Ceria Catalysts via Atom Trapping. *Science* **2016**, *353* (6295), 150–154.

(10) Zhu, C.; Fu, S.; Shi, Q.; Du, D.; Lin, Y. Single-Atom Electrocatalysts. *Angew. Chem. Int. Ed.* **2017**, *56* (45), 13944–13960.

(11) Li, Z.; Wang, D.; Wu, Y.; Li, Y. Recent Advances in the Precise Control of Isolated Single-Site Catalysts by Chemical Methods. *Natl. Sci. Rev.* **2018**, *5* (5), 673–689.

(12) Wang, J.; Li, Z.; Wu, Y.; Li, Y. Fabrication of Single-Atom Catalysts with Precise Structure and High Metal Loading. *Adv. Mater.* **2018**, *30* (48), 1801649.

(13) Shi, Y.; Zhao, C.; Wei, H.; Guo, J.; Liang, S.; Wang, A.; Zhang, T.; Liu, J.; Ma, T. Single-Atom Catalysis in Mesoporous Photovoltaics: The Principle of Utility Maximization. *Adv. Mater.* **2014**, *26* (48), 8147–8153.

(14) Vajda, S.; White, M. G. Catalysis Applications of Size-Selected Cluster Deposition. *ACS Catal.* **2015**, *5* (12), 7152–7176.

(15) Yao, Y.; Huang, Z.; Xie, P.; Wu, L.; Ma, L.; Li, T.; Pang, Z.; Jiao, M.; Liang, Z.; Gao, J.; He, Y.; Kline, D. J.; Zachariah, M. R.; Wang, C.; Lu, J.; Wu, T.; Li, T.; Wang, C.; Shahbazian-Yassar, R.; Hu, L. High Temperature Shockwave Stabilized Single Atoms. *Nat. Nanotechnol.* **2019**, *14* (9), 851–857.

(16) Lin, L.; Zhou, W.; Gao, R.; Yao, S.; Zhang, X.; Xu, W.; Zheng, S.; Jiang, Z.; Yu, Q.; Li, Y.-W.; Shi, C.; Wen, X.-D.; Ma, D. Low-Temperature Hydrogen Production from Water and Methanol Using Pt/α-MoC Catalysts. *Nature* **2017**, *544* (7648), 80–83.

(17) Qiao, B.; Wang, A.; Yang, X.; Allard, L. F.; Jiang, Z.; Cui, Y.; Liu, J.; Li, J.; Zhang, T. Single-Atom Catalysis of CO Oxidation Using Pt_1/FeO_x. *Nat. Chem.* **2011**, *3* (8), 634–641.

(18) Wang, X.; Chen, W.; Zhang, L.; Yao, T.; Liu, W.; Lin, Y.; Ju, H.; Dong, J.; Zheng, L.; Yan, W.; Zheng, X.; Li, Z.; Wang, X.; Yang, J.; He, D.; Wang, Y.; Deng, Z.; Wu, Y.; Li, Y. Uncoordinated Amine Groups of Metal–Organic Frameworks to Anchor Single Ru Sites as Chemoselective Catalysts toward the Hydrogenation of Quinoline. *J. Am. Chem. Soc.* **2017**, *139* (28), 9419–9422.

(19) Yin, P.; Yao, T.; Wu, Y.; Zheng, L.; Lin, Y.; Liu, W.; Ju, H.; Zhu, J.; Hong, X.; Deng, Z.; Zhou, G.; Wei, S.; Li, Y. Single Cobalt Atoms with Precise N-Coordination as Superior Oxygen Reduction Reaction Catalysts. *Angew. Chem.* **2016**, *128* (36), 10958–10963.

(20) Lai, W.; Zhang, B.; Hu, Z.; Qu, X.; Jiang, Y.; Wang, Y.; Wang, J.; Liu, H. K.; Chou, S. The Quasi-Pt-Allotrope Catalyst: Hollow PtCo@single-Atom Pt_1 on

Nitrogen-Doped Carbon toward Superior Oxygen Reduction. *Adv. Funct. Mater.* **2019**, *29* (13), 1807340.

(21) Wu, J.; Xiong, L.; Zhao, B.; Liu, M.; Huang, L. Densely Populated Single Atom Catalysts. *Small Methods* **2020**, *4*(2), 1900540.

(22) Li, J.; Chen, S.; Yang, N.; Deng, M.; Ibraheem, S.; Deng, J.; Li, J.; Li, L.; Wei, Z. Ultrahigh-Loading Zinc Single-Atom Catalyst for Highly Efficient Oxygen Reduction in Both Acidic and Alkaline Media. *Angew. Chem. Int. Ed.* **2019**, 58 (21), 7035–7039.

(23) Li, F.; Han, G. F.; Noh, H. J.; Kim, S. J.; Lu, Y.; Jeong, H. Y.; Fu, Z.; Baek, J. B. Boosting Oxygen Reduction Catalysis with Abundant Copper Single Atom Active Sites. *Energy Environ. Sci*. **2018**, 11(8), 2263–2269.

(24) An, S.; Zhang, G.; Wang, T.; Zhang, W.; Li, K.; Song, C.; Miller, J.T.; Miao, S.; Wang, J.; Guo, X. High-Density Ultra-Small Clusters and Single-Atom Fe Sites Embedded in Graphitic Carbon Nitride (g-C3N4) for Highly Efficient Catalytic Advanced Oxidation Processes. *ACS nano* **2018**, *12* (9), 9441–9450.

(25) Liu, J.C.; Xiao, H.; Li, J. Constructing High-Loading Single-Atom/Cluster Catalysts via An ElectroChemical Potential Window Strategy. *J. Am. Chem. Soc.* **2020**, *142* (7), 3375–3383.

(26) Li, J.; Chen, S.; Quan, F.; Zhan, G.; Jia, F.; Ai, Z.; Zhang, L. Accelerated Dinitrogen Electroreduction to Ammonia via Interfacial Polarization Triggered by Single-Atom Protrusions. *Chem* **2020**, *6* (4), 885–901.

(27) Aslan, E.; Sarilmaz, A.; Yanalak, G.; Ozel, S. S.; Ozel, F.; Patir, I. H. Transition Metal–Incorporated Tungsten-Based Ternary Refractory Metal Selenides (MWSex; M = Fe, Co, Ni, and Mn) as Hydrogen Evolution Catalysts at Soft Interfaces. *Mater. Today Energy* **2020**, *18*, 100510.

(28) Liu, G.; Robertson, A. W.; Li, M. M.-J.; Kuo, W. C. H.; Darby, M. T.; Muhieddine, M. H.; Lin, Y.-C.; Suenaga, K.; Stamatakis, M.; Warner, J. H.; Tsang, S. C. E. MoS_2 Monolayer Catalyst Doped with Isolated Co Atoms for the Hydrodeoxygenation Reaction. *Nat. Chem.* **2017**, *9* (8), 810–816.

(29) González, J. R.; Alcántara, R.; Tirado, J. L.; Fielding, A. J.; Dryfe, R. A. W. Electrochemical Interaction of Few-Layer Molybdenum Disulfide Composites vs Sodium: New Insights on the Reaction Mechanism. *Chem. Mater.* **2017**, *29* (14), 5886–5895.

(30) Makarova, M.; Okawa, Y.; Aono, M. Selective Adsorption of Thiol Molecules at Sulfur Vacancies on MoS_2 (0001), Followed by Vacancy Repair via S–C Dissociation. *J. Phys. Chem. C* **2012**, *116* (42), 22411–22416.

(31) Chou, S. S.; De, M.; Kim, J.; Byun, S.; Dykstra, C.; Yu, J.; Huang, J.; Dravid, V. P. Ligand Conjugation of Chemically Exfoliated MoS_2. *J. Am. Chem. Soc.* **2013**, *135* (12), 4584–4587.

(32) Yu, Z.; Pan, Y.; Shen, Y.; Wang, Z.; Ong, Z.-Y.; Xu, T.; Xin, R.; Pan, L.; Wang, B.; Sun, L.; Wang, J.; Zhang, G.; Zhang, Y. W.; Shi, Y.; Wang, X. Towards Intrinsic Charge Transport in Monolayer Molybdenum Disulfide by Defect and Interface Engineering. *Nat. Commun.* **2014**, *5* (1), 5290.

(33) Hachtel, J. A.; Yu, S.; Lupini, A. R.; Pantelides, S. T.; Gich, M.; Laromaine, A.; Roig, A. Gold Nanotriangles Decorated with Superparamagnetic Iron Oxide Nanoparticles: A Compositional and Microstructural Study. *Faraday Discuss.* **2016**, *191*, 215–227.

(34) Petkov, V.; Billinge, S. J. L.; Larson, P.; Mahanti, S. D.; Vogt, T.; Rangan, K. K.; Kanatzidis, M. G. Structure of Nanocrystalline Materials Using Atomic Pair Distribution Function Analysis: Study of $LiMoS_2$. *Phys. Rev. B* **2002**, *65* (9), 092105.

(35) Petkov, V.; Trikalitis, P. N.; Bozin, E. S.; Billinge, S. J. L.; Vogt, T.; Kanatzidis, M. G. Structure of $V_2O_5{\cdot}nH_2O$ Xerogel solved by the atomic pair distribution function technique. *J. Am. Chem. Soc.* **2002**, *124* (34), 10157–10162.

(36) El-Bahy, G. M. .; El-Sayed, B. .; Shabana, A. . Vibrational and Electronic Studies on Some Metal Thiourea Complexes. *Vib. Spectrosc.* **2003**, *31* (1), 101–107.

(37) Wu, C.-K.; Yin, M.; O'Brien, S.; Koberstein, J. T. Quantitative Analysis of Copper Oxide Nanoparticle Composition and Structure by X-Ray Photoelectron Spectroscopy. *Chem. Mater.* **2006**, *18* (25), 6054–6058.

(38) Morris, A. J.; Hesterberg, D. L. Iron(III) Coordination and Phosphate Sorption in Peat Reacted with Ferric or Ferrous Iron. *Soil Sci. Soc. Am. J.* **2012**, *76* (1), 101–109.

(39) Cano, A.; Lartundo-Rojas, L.; Shchukarev, A.; Reguera, E. Contribution to The Coordination Chemistry of Transition Metal Nitroprussides: a cryo-XPS study. *New J. Chem.* **2019**, *43* (12), 4835–4848.

(40) Fu, C.; Zhao, G.; Zhang, H.; Li, S. A Facile Route to Controllable Synthesis of Fe_3O_4/Graphene Composites and Their Application in Lithium-Ion Batteries. *Int. J. Electrochem. Sci.* **2014**, *9* (1), 46–60.

(41) You, M.; Kim, T. G.; Sung, Y. M. Synthesis of Cu-Doped TiO_2 Nanorods with Various Aspect Ratios and Dopant Concentrations. *Cryst. Growth Des.* **2010**, *10* (2), 983–987.

(42) Giesen, M.; Jugovac, M.; Zamborlini, G.; Feyer, V.; Gunkel, F.; Mueller, D. N. Principal Component Analysis: Reveal Camouflaged Information in X-Ray Absorption Spectroscopy Photoemission Electron Microscopy of Complex Thin Oxide Films. *Thin Solid Films* **2018**, *665*, 75–84.

(43) Kim, D. H.; Han, S. W.; Yoon, H. S.; Kim, Y. D. Reverse Water Gas Shift Reaction Catalyzed by Fe Nanoparticles with High Catalytic Activity and Stability. *J. Ind. Eng. Chem.* **2015**, *23*, 67–71.

(44) Goguet, A.; Meunier, F.; Breen, J. P.; Burch, R.; Petch, M. I.; Faur Ghenciu, A. Study of the Origin of the Deactivation of a Pt/CeO_2 Catalyst during Reverse Water Gas Shift (RWGS) Reaction. *J. Catal.* **2004**, *226* (2), 382–392.

(45) Su, X.; Yang, X.; Zhao, B.; Huang, Y. Designing of Highly Selective and High-Temperature Endurable RWGS Heterogeneous Catalysts: Recent Advances and the Future Directions. *J. Energy Chem.* **2017**, *26* (5), 854–867.

(46) Fishman, Z. S.; He, Y.; Yang, K. R.; Lounsbury, A. W.; Zhu, J.; Tran, T. M.; Zimmerman, J. B.; Batista, V. S.; Pfefferle, L. D. Hard Templating Ultrathin Polycrystalline Hematite Nanosheets: Effect of Nano-Dimension on CO_2 to CO Conversion: Via the Reverse Water-Gas Shift Reaction. *Nanoscale* **2017**, *9* (35), 12984–12995.

(47) Chou, C. Y.; Loiland, J. A.; Lobo, R. F. Reverse Water-Gas Shift Iron Catalyst Derived from Magnetite. *Catalysts* **2019**, *9* (9) 773.

(42) Yang, L.; Pastor-Pérez, L.; Villora-Pico, J. J.; Gu, S.; Sepúlveda-Escribano, A.; Reina, T. R. CO_2 Valorisation via Reverse Water-Gas Shift Reaction Using Promoted Fe/CeO_2-Al_2O_3 Catalysts: Showcasing the Potential of Advanced Catalysts to Explore New Processes Design. *Appl. Catal. A Gen.* **2020**, *593*, 117442.

(43) Dai, B.; Zhou, G.; Ge, S.; Xie, H.; Jiao, Z.; Zhang, G.; Xiong, K. CO_2 Reverse Water-Gas Shift Reaction on Mesoporous M-CeO_2 Catalysts. *Can. J. Chem. Eng.* **2017**, *95* (4), 634–642.

(48) Kaŝpar, J.; Graziani, M.; Rahman, A. M.; Trovarelli, A.; Vichi, E. J. S.; da Silva, E. C. Carbon Dioxide Hydrogenation over Iron Containing Catalysts. *Appl. Catal. A, Gen.* **1994**, *117* (2), 125–137.

(49) Kim, S. S.; Lee, H. H.; Hong, S. C. A Study on the Effect of Support's Reducibility on the Reverse Water-Gas Shift Reaction over Pt Catalysts. *Appl. Catal. A Gen.* **2012**, *423–424*, 100–107.

(50) Kwak, J. H.; Kovarik, L.; Szanyi, J. Heterogeneous Catalysis on Atomically Dispersed Supported Metals: CO_2 Reduction on Multifunctional Pd Catalysts. *ACS Catal.* **2013**, *3* (9), 2094–2100.

(51) Wang, C.; Guan, E.; Wang, L.; Chu, X.; Wu, Z.; Zhang, J.; Yang, Z.; Jiang, Y.; Zhang, L.; Meng, X.; Gates, B. C.; Xiao, F. S. Product Selectivity Controlled by Nanoporous Environments in Zeolite Crystals Enveloping Rhodium Nanoparticle Catalysts for CO_2 Hydrogenation. *J. Am. Chem. Soc.* **2019**, *141* (21), 8482–8488.

(52) Kim, R.; Kim, J.; Do, J. Y.; Seo, M. W.; Kang, M. Carbon Dioxide Photoreduction on The Bi_2S_3/MoS_2 Catalyst. *Catalysts* **2019**, *9* (12), 998.

(53) Jiang, H.; Caro, J. Interfacial Au/MoC Catalyst for Low-Temperature Water-Gas Shift Reaction. *Chem* **2017**, *3*(2), 209–210.

(54) Zhu, L.; Lin, H.; Li, Y.; Liao, F.; Lifshitz, Y.; Sheng, M.; Lee, S. T.; Shao, M. A Rhodium/Silicon co-Electrocatalyst Design Concept to Surpass Platinum Hydrogen Evolution Activity at High Overpotentials. *Nature Commun.* **2016**, *7*, 12272.

(55) Jing, H.; Li, Q.; Wang, J.; Liu, D.; Wu, K. Theoretical Study of The Reverse Water Gas Shift Reaction on Copper Modified β-Mo_2C (001) Surfaces. *J. Phys. Chem. C* **2019**, *123*(2), 1235−1251.

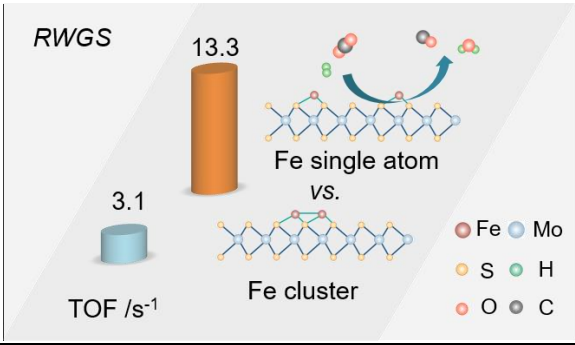
RWGS
13.3
Fe single atom
vs.
3.1
Fe cluster
TOF /s-1
Fe
Mo
S
H
O
C